Ultramicroscopy 193 (2018) 84–89

Contents lists available at ScienceDirect

Ultramicroscopy

journal homepage: www.elsevier.com/locate/ultramic

Multiple strains and polar states in $PbZr_{0.52}Ti_{0.48}O_3/PbTiO_3$ superlattices revealed by aberration-corrected HAADF-STEM imaging

Tang Y.L.[a], Zhu Y.L.[a], Wang Y.J.[a], Ma X.L.[a,b,*]

[a] Shenyang National Laboratory for Materials Science, Institute of Metal Research, Chinese Academy of Sciences, Wenhua Road 72, Shenyang, Liaoning 110016, China
[b] State Key Lab of Advanced Processing and Recycling on Non-ferrous Metals, Lanzhou University of Technology, Lanzhou 730050, China

ARTICLE INFO

Keywords:
Aberration-corrected high angle annular dark field (HAADF)
Ferroelectric film
$PbZr_{0.52}Ti_{0.48}O_3/PbTiO_3$ superlattice
Multiple strain states
Polarization enhancement

ABSTRACT

Tuning multiple strain and polar states of ferroelectrics by using strain engineering is an essential approach for designing multifunctional electric devices such as multiple state memories. However, integrating multiple strain states is still a challenge, and in addition, revealing such strains and the resultant polar behaviors on the atomic level remains difficult. In this work we prepare $PbZr_{0.52}Ti_{0.48}O_3/PbTiO_3$ (PZT/PTO) superlattices on $SrRuO_3$-buffered $SrTiO_3$(001) substrates. Aberration-corrected high angle annular dark field scanning transmission electron microscopy (HAADF-STEM) reveals that the superlattice is coherent in both *c* (out-of-plane polar direction) and *a* (in-plane polar direction) domains. We find that the strain states of both PZT and PTO in *c* and *a* domains are variant, leading to four special strain states. For example, the tetragonality for PTO in *c* and *a* domains is 1.061 and 1.045, respectively. In contrast, PZT in *c* domains displays a tetragonality as giant as 1.107, which corresponds to 110 μC cm^{-2} spontaneous polarization, much larger than the bulk PZT; while PZT in *a* domains exhibits 1.010 tetragonality with about 70 μC cm^{-2} polarization. This study reveals a practical way to integrate multiple strain states and enhanced polarizations in ferroelectric films, which could be used as multifunctional electric elements.

1. Introduction

Design and preparation of ferroelectric superlattice (SL) is an effective way to tailor properties of ferroelectric materials with artificial structures and responses [1–5]. For instance, unusual thermodynamic phase transition sequence and nonergodicity were predicted in ferroelectric $Pb(Zr_{1-x1}Ti_{x1})O_3/Pb(Zr_{1-x2}Ti_{x2})O_3$ SLs [1]. Thickness-driven antiferroelectric to ferroelectric transition of $PbZrO_3$ layer in $PbZrO_3/Pb(Zr_{0.8}Ti_{0.2})O_3$ SL was identified with orthorhombic to rhombohedral phase transition [2]. In addition, domain structures in ferroelectric SLs were found to be strongly related to the thickness of each individual ferroelectric layer, where tetragonal *a* domains (in-plane polar directions) could penetrate the rhombohedral ground state of $PbZr_{0.6}Ti_{0.4}O_3$ layer when each layer thickness of $Pb(Zr_{0.4}Ti_{0.6})O_3/Pb(Zr_{0.6}Ti_{0.4})O_3$ SLs was thinner than a specific value [3]. Particularly, except for a few interfaces near the $SrTiO_3$ substrate, all the above SLs were found to be completely coherent in both *c* (out-of-plane polar directions) and *a* domains for $Pb(Zr_{0.4}Ti_{0.6})O_3/Pb(Zr_{0.6}Ti_{0.4})O_3$ and $Pb(Zr_{0.2}Ti_{0.8})O_3/Pb(Zr_{0.4}Ti_{0.6})O_3$ SLs, although large mismatches are involved here [3–5]. Macroscopically, remnant polarization and dielectric constant could be wildly modulated by varying the thickness configurations of these ferroelectric SLs, where enhanced electrical properties could be achieved in SLs with specific thickness arrangements [4]. However, it is still difficult to reveal the atomic structures and strain distributions in these coherent ferroelectric SLs, since in both *a* and *c* domains there are two ferroelectric materials with completely different lattice parameters. Moreover, further impact of atomic structures on the polar distributions and macroscopic polarization in these ferroelectric SLs is even more elusive.

In this paper, the fine atomic structures and strain distributions in $PbZr_{0.52}Ti_{0.48}O_3/PbTiO_3$ (PZT/PTO) SL were quantitatively studied based on aberration corrected high angle annular dark field scanning transmission electron microscopy (HAADF-STEM) [6–9]. We found that the SL was coherent in both *c* and *a* domains, where both the PZT and PTO unit cells in *c* and *a* domains exhibit different strain states and special four strain states were thus established. Particularly, giant tetragonality was identified in *c* domains in PZT layers, accompanied with largely enhanced spontaneous polarizations. In contrast, *a* domains in PZT layers exhibit a reduced tetragonality compared with the bulk PZT. However, large spontaneous polarization is still maintained here.

This study shows that the aberration corrected HAADF-STEM is an effective way to reveal atomic structures and polar distributions in

* Corresponding author at: Shenyang National Laboratory for Materials Science, Institute of Metal Research, Chinese Academy of Sciences, Wenhua Road 72, Shenyang, Liaoning 110016, China.
E-mail address: xlma@imr.ac.cn (X.L. Ma).

https://doi.org/10.1016/j.ultramic.2018.06.012
Received 14 January 2018; Received in revised form 13 April 2018; Accepted 15 June 2018
Available online 18 June 2018

ferroelectric SLs. Moreover, these results reveal practical methods to integrate multiple strain/polar states and polarization enhancement in ferroelectric films, which could be potentially used as multifunctional electric elements.

2. Material and methods

The $[PbZr_{0.52}Ti_{0.48}O_3/PbTiO_3]_{15}$ SLs were deposited on $SrRuO_3$ buffered $SrTiO_3(001)$ substrates by pulsed laser deposition (PLD), using a KrF ($\lambda = 248$ nm) excimer laser. The growth temperature is 575 °C and 0.3 mbar oxygen pressure, a laser energy of 2 J·cm^{-2}, a pulse rate of 5 Hz were used for deposition [5]. Cross-sectional samples for the STEM experiments were prepared by slicing, gluing, grinding, dimpling, and finally ion milling. A Gatan PIPS was used for the final ion milling. HAADF-STEM images were recorded using an aberration-corrected STEM (Titan Cubed 60–300 kV microscope (FEI) fitted with a high-brightness field-emission gun (X-FEG) and double Cs corrector from CEOS) operating at 300 kV. The diffraction contrast image was recorded using a conventional TEM (Tecnai G2 F30 (FEI) working at 300 kV). The acquisition durations of all HAADF-STEM images used here were 40 s. The beam convergence angle is 25 mrad, and the collection angle ranges from 50 mrad to 250 mrad. The raw digital images were set to 2048 pixel × 2048 pixel when acquired. All the lattice parameters were measured along the fast scan direction. HAADF-STEM images were acquired along in-plane [100] direction so that possible 90° domain walls could be imaged. Along the [100] direction, Ti or Zr/Ti atoms are somewhat overlapped with O atoms in $PbTiO_3$ or $PbZr_{0.52}Ti_{0.48}O_3$ unit cells. For determining the lattice parameters and Zr/Ti displacements ($\delta_{Zr/Ti}$), noise in the HAADF images was filtered by Wiener filtering. The atom positions were determined accurately by fitting them as 2D Gaussian peaks by using Matlab [8–11]. The $\delta_{Zr/Ti}$ was estimated as a spacing between each Zr/Ti^{4+}-O^{2-} and the center of mass of its four nearest neighbors Pb^{2+}, since the O atom has little effect on the location of Zr/Ti columns under HAADF-STEM mode [12]. The visualization of the strains and lattice rotations was carried out using Gatan Digital Micrograph software.

3. Results

3.1. General information

At room temperature, $PbZr_{0.52}Ti_{0.48}O_3$ crystal has a tetragonal structure with lattice parameters $a = b = 4.036$ Å and $c = 4.146$ Å [13]. $PbTiO_3$ crystal has a tetragonal structure with lattice parameters $a = b = 3.900$ Å and $c = 4.148$ Å [14]. $SrRuO_3$ has a quasicubic lattice parameter $a = 3.928$ Å [15]. $SrTiO_3$ substrate has a cubic structure with lattice parameter $a = 3.905$ Å [13,15]. Fig. 1 shows a dark field TEM image of the PZT/PTO SL on a $SrRuO_3$ buffered $SrTiO_3(001)$ substrate. It is seen that the layered structures are well identified, indicating that a high quality ferroelectric SL was obtained. Moreover, obvious stripe domains evolved in the SL, which might be the 90° domains (*a* domains). Nevertheless, it is difficult to extract more detailed information from the dark field imaging technique. Thus we perform aberration-corrected HAADF-STEM imaging to reveal the atomic details of the SL, since this is an accurate method to record atomic structures without the need of taking too much into account of the thickness of materials.

3.2. Atomic structures and lattice parameters revealed by HAADF-STEM

Fig. 2 shows high resolution HAADF-STEM images of the PZT/PTO SL. We find that the wide domains in Fig. 1 are *c* domains (Fig. 2(a)), while the narrow domains are *a* domains, as marked in Fig. 2(b). The fast scan directions for Fig. 2(a) and (b) are along the horizontal direction. We find that the first PTO/$SrRuO_3$ interface is completely coherent, while there are some $a < 100 >$ type misfit dislocations at the first PZT/PTO interface. These phenomena can be explained in terms of the fact that the mismatch between PTO and $SrRuO_3$ is small ($\sim -0.7\%$), while the mismatch between PZT and PTO is large ($\sim 3.4\%$). However, all the other PZT/PTO SL interfaces above the first PZT/PTO layer are completely coherent again, indicating the relaxation through the $a < 100 >$ misfit dislocations was just restricted at the first PZT/PTO interfaces. Thus the fine lattice and polar characters in the above PZT/PTO SL would be completely different from the first PZT/PTO layer, which are further quantitatively analyzed in the following.

First we try to identify the PZT and PTO layers embedded in the coherent SL. Although the atomic number differences are not so significant, we can distinguish the PZT and PTO layers by using the Zr/Ti-O columns intensities, as shown in Fig. 2(c). Thus the PZT and PTO layers can be preliminarily marked in Fig. 2.

To quantitatively reveal the atomic structures and polar details, the Pb^{2+} and Zr/Ti^{4+}-O^{2-} columns in the HAADF-STEM images were further analyzed. The lattice parameters were calculated along the fast scan direction, by using the atom column positions of Pb^{2+}. All the lattice parameters were calibrated by using a HAADF-STEM image of the $SrTiO_3(001)$ substrate lattice, also along the fast scan direction. All the conditions for acquiring the HAADF-STEM images of the SL and the $SrTiO_3(001)$ substrate were kept the same, so that the 0.3905 nm of the $SrTiO_3$ cubic lattice parameter can be used for calibrating and obtaining the lattice parameters of the PZT/PTO SL.

We find that the in-plane lattice parameter in the *c* domain is constant and this is the same for both PZT and PTO, as shown in Fig. 3(a). The in-plane lattice parameters in the *a* domains show the same feature. Fig. 3(b) shows the lattice parameter distributions in *c* and *a* domains. The constant values can be seen directly, where the averaged in-plane lattice for the *c* domain is 0.393 nm, while the averaged in-plane lattice for the *a* domain is 0.414 nm. It should be noted that these two values are different from all the bulk lattice parameters of the PZT and PTO

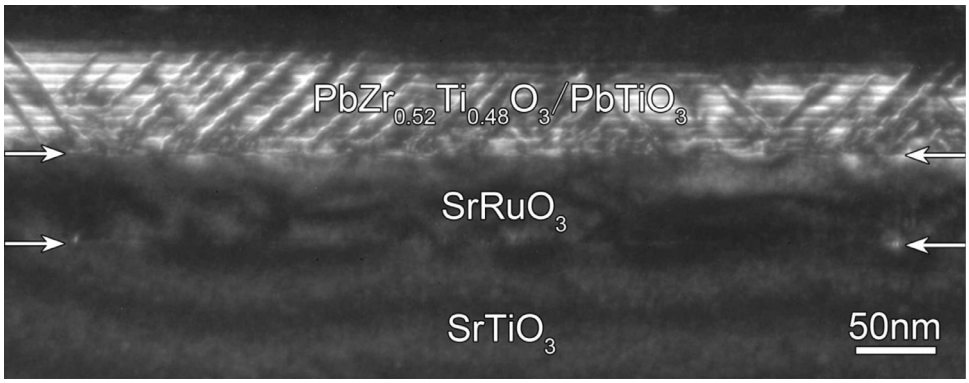

Fig. 1. Dark field TEM image of the $PbZr_{0.52}Ti_{0.48}O_3/PbTiO_3$ (PZT/PTO) superlattice on $SrRuO_3$ buffered $SrTiO_3(001)$ substrate. White arrows mark the $PbTiO_3$/$SrRuO_3$ and $SrRuO_3$/$SrTiO_3$ interfaces. Note that possible 90° domains (*a* domains) evolved in the superlattice.

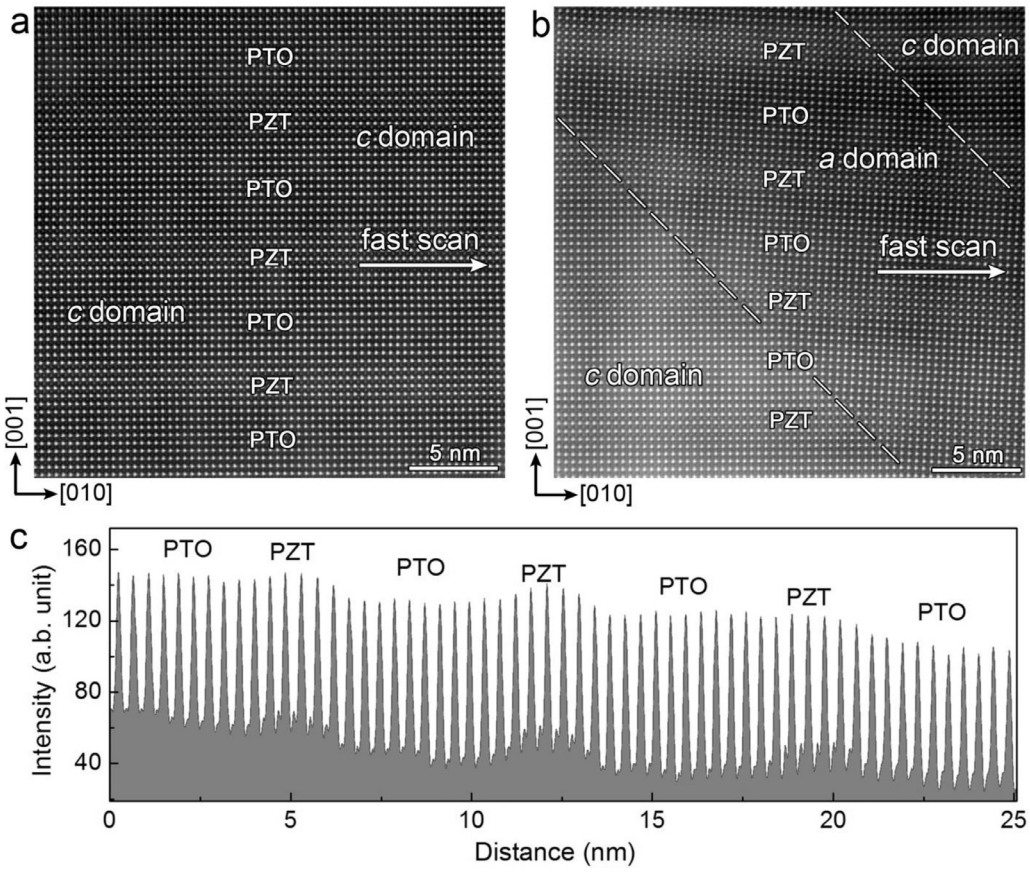

Fig. 2. High resolution HAADF-STEM imaging of the PZT/PTO superlattice. (a) HAADF-STEM image of a *c*-domain. (b) HAADF-STEM image showing co-existence of *c*-domain and *a*-domain. The fast scan of STEM imaging for (a) and (b) are along the horizontal direction. (c) HAADF-STEM image intensity distribution along the out-of-plane direction of (a). Note the PZT layers can be identified according to the B site ion intensity peaks, where the Zr/Ti-O columns in PZT layers are brighter than the Ti columns in PTO layers. Thus the PZT and PTO layers can be preliminarily identified.

crystals. These preliminary results indicate that some unusual lattice behaviors must occur here and further analysis of the out-of-plane lattice features should be performed.

Fig. 4(a) shows a HAADF-STEM image containing an *a* domain. The fast scan was tuned to be along the vertical direction so that the effects of scanning noise on the determination of the out-of-plane lattice can be minimized. Fig. 4(b) is the out-of-plane lattice map based on the HAADF-STEM image. The PZT layers exhibiting obviously larger lattice parameters can be identified directly in both *c* and *a* domains here. Fig. 5(a) shows the quantitative out-of-plane lattice distributions in the *c* and *a* domains. The peak values in the PZT layers can be seen clearly. Note that the in-plane lattice in the *a* domains actually is *c* lattice while the out-of-plane lattice in the *a* domains actually is *a* lattice. Thus the tetragonalities, that is, the *c* lattice and *a* lattice ratios (*c*/*a*), can be statistically analyzed, as shown in Fig. 5(b). Here the *a* lattice parameter for both PZT and PTO in the *c* domains is 0.393 nm, while the *c* lattice parameter for both PZT and PTO in the *a* domains is 0.414 nm (Fig. 3(b)). It can be seen that the *c*/*a* in the PZT layers show extreme values which are completely different from the bulk value 1.027. PZT unit cells in the *c* domains show a peak *c*/*a* value as large as ~1.12,

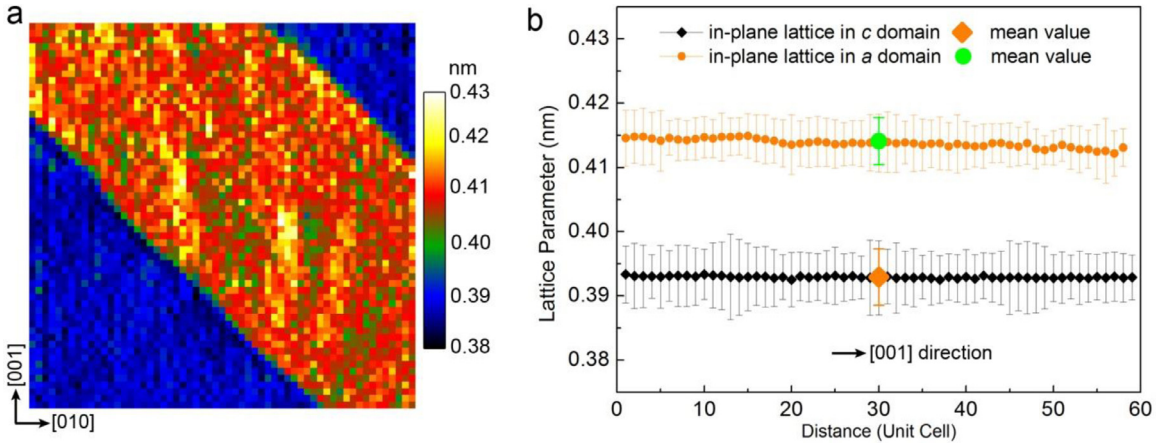

Fig. 3. In-plane lattice parameter analysis based on the HAADF-STEM imaging. (a) In-plane lattice map of Fig. 2(b). (b) In-plane lattice parameter distributions in *c* and *a* domains. Note that both the in-plane lattice parameters in *c* and *a* domains are basically constants, which are 0.414 nm and 0.393 nm, respectively. The in-plane lattice analysis was extracted from Fig. 2(a) and (b), where the in-plane fast scan direction could largely reduce the effects of STEM imaging. A high resolution HAADF-STEM image with the same magnification as Fig. 2(a) and (b) was acquired in which the $SrTiO_3$ substrate lattice was used for calibration of the lattice parameters in Fig. 3(b).

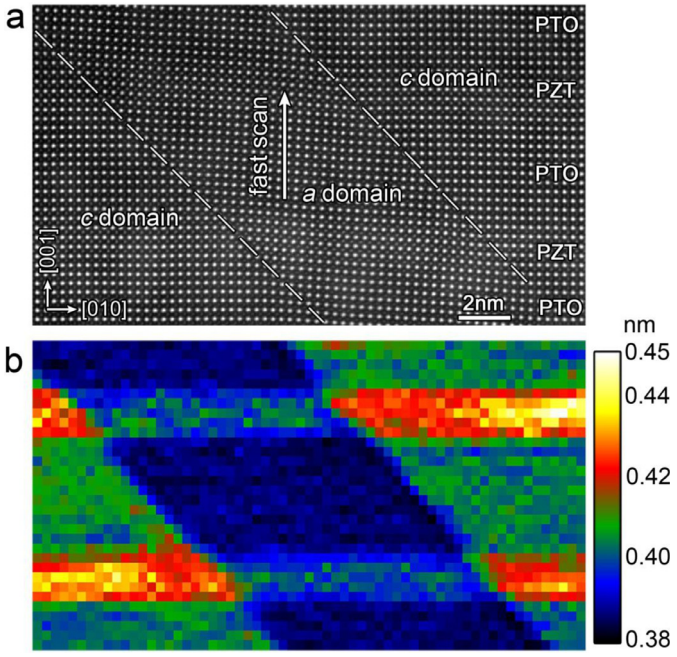

Fig. 4. Out-of-plane lattice parameter analysis based on HAADF-STEM imaging. (a) High resolution HAADF-STEM image contains both *c* and *a* domains. The fast scan of STEM imaging is along the vertical direction, which could largely reduce the effects of scanning noise on out-of-plane lattice determinations. (b) Out-of-plane lattice map of (a). Note that both the out-of-plane lattice parameters of PZT layers in *c* and *a* domains are enlarged compared with those of PTO layers.

while PZT unit cells in the *a* domains show minimum *c*/*a* value close to 1. In contrast, the *c*/*a* values for PTO unit cells in *c* and *a* domains are more close to the bulk PTO. Nevertheless, slight differences can also be identified. Averaged *c*/*a* values for PTO unit cells in the *c* domains and *a* domains are 1.061 and 1.045, respectively. Thus it is clear that the PZT/PTO SL here displays a special four strain state, where both PZT and PTO unit cells in the *c* and *a* domains show different strain states.

It is known that the polarization and strain are strongly coupled with each other in tetragonal ferroelectrics [16–21]. Thus it is of great significance to analyze the ferroelectric ion displacements in this PZT/PTO SL, since the Zr/Ti ion displacement ($\delta_{Zr/Ti}$) is directly associated with the spontaneous polarizations (***P***s) in each unit cell. Here the $\delta_{Zr/Ti}$ will be somewhat affected since along [100] direction the Zr/Ti-O columns were recorded actually. Nevertheless, our previous work has revealed that in PTO unit cell the δ_{Ti} is less affected by the O atoms under HAADF-STEM mode [12]. Thus the magnitude of $\delta_{Zr/Ti}$ can be roughly estimated by using the measured $\delta_{Zr/Ti\text{-}O}$ directly from a HAADF-STEM image. Fig. 6(a) and (b) show the estimated in-plane and out-of-plane $\delta_{Zr/Ti}$ components, respectively. We further statistically analyzed the $\delta_{Zr/Ti}$ values in *c* and *a* domains, as shown in Fig. 6(c). It is seen that the $\delta_{Zr/Ti}$ in *a* domain is basically uniform, indicating that there is little difference of ***P***s between PZT and PTO in *a* domains. The averaged $\delta_{Zr/Ti}$ values for PZT and PTO unit cells in *a* domain are 0.013(5) nm and 0.012(4) nm, respectively, which correspond to ***P***s value of about 70 μC cm^{-2} (according to the linear relationship between $\delta_{Zr/Ti}$ and ***P***s, where ***P***s = 1.96k·$\delta_{Zr/Ti}$ and k = 2726 (μC·cm^{-2}) nm^{-1}, refs. 17,21)

In contrast, we find large enhancement of $\delta_{Zr/Ti}$ in PZT unit cells within the *c* domains, which is consistent with the large *c*/*a* ratio here. The averaged $\delta_{Zr/Ti}$ values for PZT and PTO unit cells in *c* domain are 0.021(1) nm and 0.017(4) nm, respectively, which correspond to ***P***s value of about 110 μC cm^{-2} and 90 μC cm^{-2}. The lattice parameters and ferroelectric ion displacements in PZT and PTO unit cells within *c* and *a* domains are summarized in Table 1.

4. Discussion

It is well known that in single layer, single composition epitaxial systems, mismatches can be easily relaxed when films get thicker [22], especially for large mismatch systems, where the critical thicknesses of epitaxial films could be less than several unit cells [22]. However, present work reveals that superlattice growth is an effective way to preserve large strains in ferroelectric films. Here the mismatch between $PbZr_{0.52}Ti_{0.48}O_3$ and $PbTiO_3$ is ~3.4%, which should yield a critical

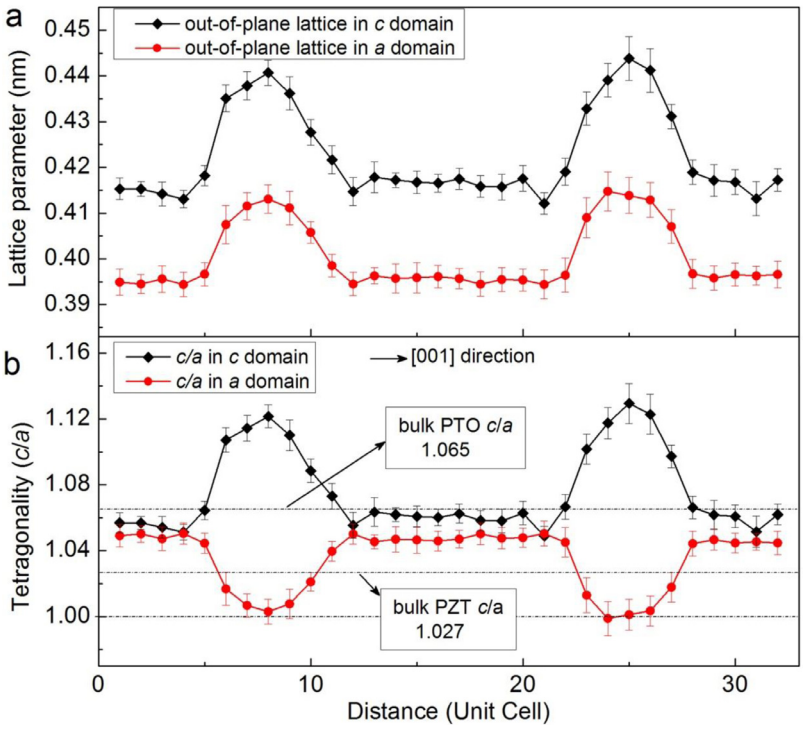

Fig. 5. Out-of-plane lattice parameter analysis based on Fig. 4(a). (a) Out-of-plane lattice parameter distributions in *c* and *a* domains. (b) Tetragonality (*c*/*a* ratio) distributions in *c* and *a* domains. Here the tetragonality was calculated as follows: for the *c* domain, the *c* lattice parameters correspond to the black cure shown in (a), while the *a* lattice parameter is a constant as 0.393 nm shown in Fig. 3(b); for the *a* domain, the *a* lattice parameters correspond to the red cure shown in (a), while the *c* lattice parameter is a constant as 0.414 nm shown in Fig. 3(b). Note that both the out-of-plane lattice parameters for the PZT layers in *c* and *a* domains are enlarged compared with those of PTO layers. Also note the severe differences of tetragonalities for PZT unit cells in *c* and *a* domains, while those differences for PTO unit cells are smaller.

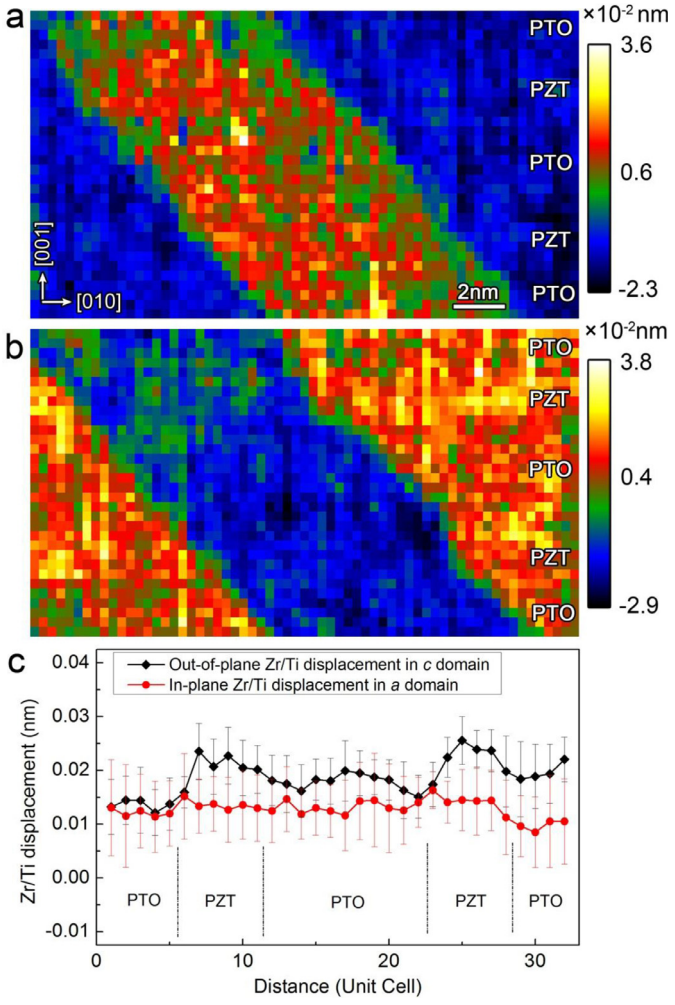

Fig. 6. Zr/Ti off center displacement analysis based on Fig. 4(a). (a) In-plane Zr/Ti displacement map. (b) Out-of-plane Zr/Ti displacement map. (c) Out-of-plane and in-plane Zr/Ti displacement distributions in *c* and *a* domains. Note the Zr/Ti displacement in PZT layer is increased in *c* domain, while the Zr/Ti shift in *a* domain remains constant.

Table 1
Parameter summary of the superlattice.

	lattice *a* (nm)	lattice *c* (nm)	*c*/*a*	Zr/Ti shift (nm)	***P***s (μC·cm^{-2})
PTO in *c* domain	0.393	0.417	1.061	0.017(4)	93
PZT in *c* domain	0.393	0.435	1.107	0.021(1)	113
PTO in *a* domain	0.396	0.414	1.045	0.012(4)	66
PZT in *a* domain	0.410	0.414	1.010	0.013(5)	72

thickness around 4 unit cells according to previous works [22]. However, in the present $PbZr_{0.52}Ti_{0.48}O_3/PbTiO_3$ superlattice system, each period contains ~18 unit cells of $PbZr_{0.52}Ti_{0.48}O_3/PbTiO_3$ which are free of any dislocations. Except for the first $PbZr_{0.52}Ti_{0.48}O_3/PbTiO_3$ period just above the $SrRuO_3$ buffer layer, the entire above $PbZr_{0.52}Ti_{0.48}O_3/PbTiO_3$ superlattice is coherent.

Moreover, the as-grown coherent ferroelectric superlattice displays clear four strain states, where both the $PbZr_{0.52}Ti_{0.48}O_3$ and $PbTiO_3$ in *c* and *a* domains show different *c*/*a* ratios (Table 1). These results are completely different from single composition tetragonal films, where the lattice of $PbZr_xTi_{1-x}O_3$ in *c* and *a* domains is actually the same [23,24]. In particular, giant *c*/*a* ratio (~1.107) are obtained in $PbZr_{0.52}Ti_{0.48}O_3$ layer within the *c* domain, which is much larger than the bulk $PbZr_{0.52}Ti_{0.48}O_3$ crystal (1.027).

In addition, since the polarization and *c*/*a* are strongly coupled with each other in these tetragonal ferroelectrics [16–21], we can further analyze the polar character in the ferroelectric superlattice. First we note that the *c*/*a* for $PbTiO_3$ in the *c* domain is ~1.061 with δ_{Ti} of 0.017(4) nm, where both *c*/*a* and δ_{Ti} are close to the bulk $PbTiO_3$ lattice (*c*/*a* = 1.065, δ_{Ti} = 0.017 nm, ref. 17). Thus the ***P***s in *c* domain $PbTiO_3$ can be estimated as ~ 90 μC cm^{-2}, which is consistent with the result estimated by Glazer and Mabud [17]. This value can be understood as the ideal ***P***s of $PbTiO_3$ crystal, since the actually measured ***P***s for $PbTiO_3$ is always lower than this value as 75 μC cm^{-2}. The real experiment measurement of ***P***s can be easily underestimated because of defects and the contact condition between ferroelectrics and electrodes [15]. Thus the ideal ***P***s of $PbTiO_3$ is about 20% larger than the measured value.

Now we analyze the polarization enhancement in the $PbZr_{0.52}Ti_{0.48}O_3$ layer within the *c* domain. We note that the measured ***P***s of $PbZr_{0.52}Ti_{0.48}O_3$ are between 40 and 50 μC cm^{-2} (refs. [16,18–20,25,26]). We assume that the measured ***P***s equals to 45 μC cm^{-2}. By using the increased percentage (~20%) of ideal ***P***s relative to measured ***P***s of $PbTiO_3$, the ideal ***P***s of $PbZr_{0.52}Ti_{0.48}O_3$ can be roughly estimated as 45·(1 + 20%) = 54 μC cm^{-2}. In present study, the giant *c*/*a* ratio (~1.107) is identified in $PbZr_{0.52}Ti_{0.48}O_3$ layer within the *c* domain, which yields large ferroelectric ion displacement as 0.021(1) nm. The corresponding ***P***s value is ~110 μC cm^{-2}, which is approximately as twice as that estimated for the ideal ***P***s of bulk $PbZr_{0.52}Ti_{0.48}O_3$.

On the other hand, the ***P***s (~66 μC cm^{-2}, Table 1) in $PbTiO_3$ layer within the *a* domain is somewhat reduced compared with the ideal value. This is reasonable since the *c*/*a* (1.045) also decreases here. However, the ***P***s in $PbZr_{0.52}Ti_{0.48}O_3$ layer here still maintains a high value (~72 μC cm^{-2}, Table 1) while its *c*/*a* is very small (1.010, Table 1). This might be due to the impact of its neighboring $PbTiO_3$ layers. The polarization of these tetragonal ferroelectrics arises from the ion displacement, which is directly associated with local atom bonding through oxygen octahedra [27]. While the $PbZr_{0.52}Ti_{0.48}O_3$ layer here tends to reduce $\delta_{Zr/Ti}$ in respond to its lowered *c*/*a*, the neighboring $PbTiO_3$ layers would push the sandwiched $PbZr_{0.52}Ti_{0.48}O_3$ layer to maintain a similar $\delta_{Zr/Ti}$ value to that of $PbTiO_3$ via lateral atom bonding. We note that the atom bonding arrangement in the *a* domain here is different from that of *c* domain. There is no such lateral atom bonding between $PbZr_{0.52}Ti_{0.48}O_3$ and $PbTiO_3$ in *c* domains, thus $PbZr_{0.52}Ti_{0.48}O_3$ and $PbTiO_3$ here tend to maintain their own ***P***s values. In other words, the polar crosstalk only tends to occur at the $PbZr_{0.52}Ti_{0.48}O_3/PbTiO_3$ interfaces, not the whole SL structure in the *c* domains. Particularly, it is noted that the ***P***s in $PbZr_{0.52}Ti_{0.48}O_3$ layer within the *a* domains is even bigger than the bulk value. Thus all the $PbZr_{0.52}Ti_{0.48}O_3$ unit cells in the ferroelectric superlattice exhibit enhanced polarizations.

Thus the present results offer a practical way to integrate multiple strain states into ferroelectric films. Moreover, these strain states further induce multiple polarization states inside the ferroelectric superlattice, which can be potentially used as multiple state ferroelectric memory elements [28,29]. In addition, giant polarization enhancement up to ~200% was identified in the $PbZr_{0.52}Ti_{0.48}O_3$ layers, which indicates novel method to largely increase ferroelectric polarization of ferroelectric films. These results directly confirm the previous observation of enhanced electrical properties in $PbZr_{0.2}Ti_{0.8}O_3/PbZr_{0.4}Ti_{0.6}O_3$ superlattices [4], where X-ray revealed some unusual strain state but it had never been directly visualized.

5. Conclusion

Atomic structures and strain states of $PbZr_{0.52}Ti_{0.48}O_3/PbTiO_3$ superlattice were analyzed through aberration-corrected HAADF-STEM. Multiple strain states exhibiting several polarizations were found in the superlattice. Large tetragonality of 1.107, in response to the clamping effects of neighboring $PbTiO_3$ layers, was identified for $PbZr_{0.52}Ti_{0.48}O_3$ layer embedded in *c* domains, which displays giant polarization enhancement up to ~200%. Our results show that aberration-corrected HAADF-STEM is an effective way to study atomic and polar characters of ferroelectric superlattices. Particularly, present work indicates novel method to integrate multiple strain/polarization states into ferroelectric films with increased polarizations, which can be potentially used as novel ferroelectric devices with enhanced responses.

Acknowledgments

This work is supported by the National Natural Science Foundation of China (No. 51501194, 51571197, 51671194, 51401212 and 51521091), National Basic Research Program of China (2014CB921002), and the Key Research Program of Frontier Sciences CAS (QYZDJ-SSW-JSC010). Y. L. T. acknowledges the IMR SYNL-T. S. Kê Research Fellowship and the Youth Innovation Promotion Association CAS (No. 2016177). We thank the Max-Planck Institute of Microstructure Physics for the thin film preparation.

References

[1] I.A. Kornev, L. Bellaiche, Unusual thermodynamic properties and nonergodicity in ferroelectric superlattices, Phys. Rev. Lett. 91 (2003) 116103.
[2] K. Boldyreva, L. Pintilie, A. Lotnyk, I.B. Misirlioglu, M. Alexe, D. Hesse, Thickness-driven antiferroelectric-to-ferroelectric phase transition of thin $PbZrO_3$ layers in epitaxial $PbZrO_3/Pb(Zr_{0.8}Ti_{0.2})O_3$ multilayers, Appl. Phys. Lett. 91 (2007) 122915.
[3] I. Vrejoiu, Y. Zhu, G.L. Rhun, M.A. Schubert, D. Hesse, M. Alexe, Structure and properties of epitaxial ferroelectric $PbZr_{0.4}Ti_{0.6}O_3/PbZr_{0.6}Ti_{0.4}O_3$ superlattices grown on $SrTiO_3$(001) by pulsed laser deposition, Appl. Phys. Lett. 90 (2007) 072909.
[4] L. Feigl, S.J. Zheng, B.I. Birajdar, B.J. Rodriguez, Y.L. Zhu, M. Alexe, D. Hesse, Impact of high interface density on ferroelectric and structural properties of $PbZr_{0.2}Ti_{0.8}O_3/PbZr_{0.4}Ti_{0.6}O_3$ epitaxial multilayers, J. Phys. D: Appl. Phys. 42 (2009) 085305.
[5] Y.L. Zhu, S.J. Zheng, X.L. Ma, L. Feigl, M. Alexe, D. Hesse, I. Vrejoiu, Microstructural evolution of $[PbZr_xTi_{1-x}O_3/PbZr_yTi_{1-y}O_3]$n epitaxial multilayers (x/y= 0.2/0.4, 0.4/0.6)–dependence on layer thickness, Philos. Mag. 90 (2010) 1359–1372.
[6] P. Gao, R. Ishikawa, B. Feng, A. Kumamoto, N. Shibata, Y. Ikuhara, Atomic-scale structure relaxation, chemistry and charge distribution of dislocation cores in $SrTiO_3$, Ultramicroscopy 184 (2018) 217–224.
[7] S.J. Pennycook, D. Jesson, High-resolution Z-contrast imaging of crystals, Ultramicroscopy 37 (1991) 14–38.
[8] C.T. Nelson, B. Winchester, Y. Zhang, S.-J. Kim, A. Melville, C. Adamo, C.M. Folkman, S.-H. Baek, C.-B. Eom, D.G. Schlom, L.-Q. Chen, X. Pan, Spontaneous vortex nanodomainarrays at ferroelectric heterointerfaces, Nano Lett. 11 (2011) 828–834.
[9] P. Gao, C.T. Nelson, J.R. Jokisaari, S.-H. Baek, C.W. Bark, Y. Zhang, E. Wang, D.G. Schlom, C.-B. Eom, X. Pan, Revealing the role of defects in ferroelectric switching with atomic resolution, Nat. Commun. 2 (591) (2011) 1600.
[10] S.M. Anthony, S. Granick, Image analysis with rapid and accurate two-dimensional Gaussian fitting, Langmuir 25 (2009) 8152–8160.
[11] C.-L. Jia, S.-B. Mi, K. Urban, I. Vrejoiu, M. Alexe, D. Hesse, Atomic–scale study of electric dipoles near charged and uncharged domain walls in ferroelectric films, Nat. Mater. 7 (2008) 57–61.
[12] Y. Liu, Y.L. Zhu, Y.L. Tang, X.L. Ma, An effect of crystal tilt on the determination of ions displacements in perovskite oxides under BF/HAADF-STEM imaging mode, J. Mater. Res. 32 (2017) 947–956.
[13] M.-W. Chu, I. Szafraniak, R. Scholz, C. Harnagea, D. Hesse, M. Alexe, U. Gösele, Impact of misfit dislocations on the polarization instability of epitaxial nanostructured ferroelectric perovskites, Nat. Mater. 3 (2004) 87–90.
[14] Y. Kuroiwa, S. Aoyagi, A. Sawada, J. Harada, E. Nishibori, M. Takata, M. Sakata, Evidence for Pb-O Covalency in Tetragonal PbTiO3, Phys. Rev. Lett 87 (2001) 217601.
[15] I. Vrejoiu, G.L. Rhun, L. Pintilie, D. Hesse, M. Alexe, U. Gösele, Intrinsic ferroelectric properties of strained tetragonal $PbZr_{0.2}Ti_{0.8}O_3$ obtained on layer–by–layer grown, defect–free single–crystalline films, Adv. Mater 18 (2006) 1657–1661.
[16] H. Morioka, S. Yokoyama, T. Oikawa, H. Funakubo, K. Saito, Spontaneous polarization change with Zr/(Zr + Ti) ratios in perfectly polar-axis-orientated epitaxial tetragonal $Pb(Zr,Ti)O_3$ films, Appl. Phys. Lett. 85 (2004) 3516–3518.
[17] A.M. Glazer, S.A. Mabud, Powder profile refinement of lead zireonate titanate at several temperatures. II. Pure $PbTiO_3$, ActaCryst. B 34 (1978) 1065–1070.
[18] B. Noheda, J.A. Gonzalo, L.E. Cross, R. Guo, S.-E. Park, D.E. Cox, G. Shirane, Tetragonal-to-monoclinic phase transition in a ferroelectric perovskite: The structure of $PbZr_{0.52}Ti_{0.48}O_3$, Phys. Rev. B 61 (2000) 8687–8695.
[19] J. Wang, Z. Li, J. Wang, H. He, C. Nan, Effect of thickness on the stress and magnetoelectric coupling in bilayered $Pb(Zr_{0.52}Ti_{0.48})O_3$-$CoFe_2O_4$ films, J. Appl. Phys. 112 (2012) 074110.
[20] N.A. Pertsev, V.G. Kukhar, H. Kohlstedt, R. Waser, Phase diagrams and physical properties of single-domain epitaxial $Pb(Zr_{1-x}Ti_x)O_3$ thin films, Phys. Rev. B 67 (2003) 054107.
[21] C.-L. Jia, V. Nagarajan, J.-Q. He, L. Houben, T. Zhao, R. Ramesh, K. Urban, R. Waser, Unit-cell scale mapping of ferroelectricity and tetragonality in epitaxial ultrathin ferroelectric films, Nat. Mater. 6 (2007) 64–69.
[22] P.A. Langjahr, F.F. Lange, T. Wagner, M. Rühle, Lattice mismatch accommodation in perovskite films on perovskite substrates, Acta Mater. 46 (1998) 773–785.
[23] A.R. Damodaran, S. Pandya, J.C. Agar, Y. Cao, R.K. Vasudevan, R. Xu, S. Saremi, Q. Li, J. Kim, M.R. McCarter, L.R. Dedon, T. Angsten, N. Balke, S. Jesse, M. Asta, S.V. Kalinin, L.W. Martin, Three-state ferroelastic switching and large electromechanical responses in $PbTiO_3$ thin films, Adv. Mater 29 (2017) 1702069.
[24] G. Catalan, A. Lubk, A.H.G. Vlooswijk, E. Snoeck, C. Magen, A. Janssens, G. Rispens, G. Rijnders, D.H.A. Blank, B. Noheda, Flexoelectric rotation of polarization in ferroelectric thin films, Nat. Mater. 10 (2011) 963–967.
[25] T.J. Zhu, L. Lu, X.B. Zhao, Z.G. Ji, J. Ma, Epitaxial growth and ferroelectric properties of $Pb(Zr_{0.52}Ti_{0.48})O_3/SrRuO_3$ heterostructures on exact $SrTiO_3$(001) substrates, J. Cryst. Growth 291 (2006) 385–389.
[26] M.J. Haun, E. Furman, S.J. Jang, L.E. Cross, Thermodynamic theory of the lead zirconate titanate solid solution system, part V: Theoretical calculations, Ferroelectrics 99 (1989) 63–86.
[27] R.E. Cohen, Origin of ferroelectricity in perovskite oxides, Nature 358 (1992) 136–138.
[28] W. Lü, C. Li, L. Zheng, J. Xiao, W. Lin, Q. Li, X.R. Wang, Z. Huang, S. Zeng, K. Han, W. Zhou, K. Zeng, J. Chen, W.Cao Ariando, T. Venkatesan, Multi-nonvolatile state resistive switching arising from ferroelectricity and oxygen vacancy migration, Adv. Mater 29 (2017) 1606165.
[29] D. Lee, S.M. Yang, T.H. Kim, B.C. Jeon, Y.S. Kim, J.-G. Yoon, H.N. Lee, S.H. Baek, C.B. Eom, T.W. Noh, Multilevel data storage memory using deterministic polarization control, Adv. Mater 24 (2012) 402–406.